UC San Diego
UC San Diego Previously Published Works

Title

Bisalt ether electrolytes: a pathway towards lithium metal batteries with Ni-rich cathodes

Permalink

https://escholarship.org/uc/item/6tj4131n

Journal

Energy & Environmental Science, 12(2)

ISSN

1754-5692

Authors

Alvarado, Judith
Schroeder, Marshall A
Pollard, Travis P
et al.

Publication Date

2019-02-13

DOI

10.1039/c8ee02601g

Peer reviewed

Check for updates

Bisalt ether electrolytes: a pathway towards lithium metal batteries with Ni-rich cathodes†

Judith Alvarado,‡[ab] Marshall A. Schroeder, [ID] ‡[a] Travis P. Pollard, [ID] ‡[a] Xuefeng Wang, [ID] [c] Jungwoo Z. Lee,[c] Minghao Zhang,[c] Thomas Wynn,[b] Michael Ding,[a] Oleg Borodin, [ID] *[a] Ying Shirley Meng*[bc] and Kang Xu*[a]

The electrochemical performance and mechanistic effects of incorporating two salts in an ether electrolyte in Li–metal cells were investigated experimentally and *via* molecular scale modeling. Improvements in efficiency and cycling stability over baseline electrolytes in lithium (Li) *versus* copper (Cu) cells were directly correlated to the initial Li-nucleation process, as observed *via* cryogenic-focused ion beam (cryo-FIB) prepared cross sections, which revealed that Li films deposited with the bisalt electrolyte were significantly thinner and denser than those from the baseline. This behavior was further traced back to the initial nucleation process *via* cryogenic transmission electron microscopy (cryo-TEM), which shows stark differences in the morphology and conformality of deposited Li as a function of electrolyte chemistry. X-ray photoelectron spectroscopy (XPS) indicated that the solid electrolyte interphase (SEI) formed from the bisalt electrolyte primarily consists of larger anion fragments, suggesting that the anion chemistry strongly influences the extent of reduction and resulting surface chemistry. *Ab initio* DFT-based and force field-based molecular dynamics calculations revealed the complex interplay (positioning, orientation, reactivity, kinetics) between the FSI^- and $TFSI^-$ anions in the double layer at both electrode–electrolyte interfaces and the ramifications for stabilizing these interfaces. As a result of the unique interphasial chemistry brought by this bisalt system, this electrolyte supports an unprecedented (for an ether-based electrolyte) capacity retention (>88%) after 300 cycles (~2 months of cycling) in a 4.4 V NMC622-Li cell, and a >30% improvement in capacity retention over baseline after 50 cycles in 4.4 V NMC622-Cu ''anode-free'' cells. Altogether, these results provide new insight into how the bisalt effect can be leveraged for regulating the timescale, chemistry, and extent of interfacial reactions. When balanced properly, this promotes efficient plating/deplating of Li, and potentially supports widespread implementation of high nickel content NMC cell configurations with limited or no excess lithium.

Broader context

The energy and power of lithium-based rechargeable batteries can be enhanced by coupling aggressive electrode chemistries such as lithium metal anodes with nickel-rich cathode materials (*e.g.* NMC622). However, these performance improvements come at the cost of addressing new safety concerns and cycling stability issues for electrolytes exposed to highly reactive cathode and anode surfaces. Despite the recent reports on dual salt electrolytes that show some promise in mediating these issues, insight into the interplay between multiple salt anions in determining reactivity and kinetics remains limited. In this work, we explore the performance improvements induced by two salts (LiFSI and LiTFSI) dissolved at high concentrations in an ether. Using a combination of electrochemical, spectroscopic, and computational approaches, we address this knowledge gap, and elucidate a thorough mechanistic understanding about how these two anions behave at electrode–electrolyte interfaces on both the anode and cathode. These insights will provide guidance for future electrolyte design that will eventually support advanced lithium metal battery chemistries with higher energy and power.

[a] *Electrochemistry Branch, Sensors and Electron Devices Directorate, U.S. Army Research Laboratory, Adelphi, MD 20783, USA. E-mail: oleg.a.borodin.civ@mail.mil, conrad.k.xu.civ@mail.mil*

[b] *Materials Science and Engineering, University of California San Diego, La Jolla, CA 92093, USA. E-mail: shirleymeng@ucsd.edu*

[c] *Department of NanoEngineering, University of California San Diego, La Jolla, CA 92093, USA*

† Electronic supplementary information (ESI) available. See DOI: 10.1039/c8ee02601g

‡ Equal contribution.

1. Introduction

Lithium metal batteries present an enticing solution to the aggressively evolving energy and power demands of consumer electronics and electric vehicles; however, despite nearly a half-century of efforts, serious barriers still exist for this electrode

780 | *Energy Environ. Sci.*, 2019, **12**, 780–794

This journal is © The Royal Society of Chemistry 2019

chemistry to deliver the capacity, rate capability, efficiency, and especially cycle life and safety required for commercialization. In Li-ion batteries (LIBs), these cell performance parameters are almost exclusively dictated by the solid electrolyte interphase (SEI), which forms between the graphitic anode and the electrolyte in a conformal and self-limiting manner from reduced electrolyte components, allowing Li$^+$-transport without conducting electrons.[1–3] Li metal introduces a far more reducing interface which also undergoes "infinite" volume changes during Li plating and stripping. Continuous exposure of highly reactive surface to electrolyte leads to persistent SEI growth that is plagued with chemical/morphological inhomogeneities and eventually results in dendritic or isolated Li. Thus, achieving highly reversible cycling of Li metal has become the greatest scientific challenge that the battery community presently faces.

A variety of approaches have been explored in order to address these issues,[4] including developing carbonaceous and flexible host structures for Li;[5–7] physical barriers such as polymer,[4] viscoelastic liquids[8] and solid state electrolytes to suppress dendrite formation;[9–13] flexible coatings;[14] and tuning electrode/electrolyte interphase chemistry *via* electrolyte engineering,[15–18] of which the latter is the most economically viable. Li–metal plating/stripping efficiencies in liquid electrolytes have been improved over four decades of research from 80% to 98.5%, cycling at 0.5 mA h cm^{-2} in Li *versus* Cu cells. This significant advance was achieved by moving away from highly reactive solvents (carbonate-based esters) to systems that are more cathodically stable, and by altering the lithium salt chemistry, as pioneered by Aurbach *et al.*[15,19,20] The morphology of the plated Li metal is dependent on a variety of factors involving both the salt(s) and solvent(s). The degree of salt dissociation, the strength of solvation, and the cathodic stability of the anion and solvent all dictate the resulting SEI.[21,22] In certain cases, simply increasing the salt concentration (>3 M) has enabled single solvent systems for lithium sulfur and high voltage (5.0 V) chemistries, as demonstrated by Kim *et al.*,[23] Yamada *et al.*,[24] and most recently in our work on sulfolane-based electrolytes.[25,26] Regarding the choice of solvent, electrolytes based on short ethers with low viscosity are less reactive with Li metal as compared to esters and have generally shown reduced dendrite formation.[19] Highly concentrated (4–5 M) LiFSI in 1,2 dimethoxyethane (DME) increased the Li metal cycling efficiency in Li symmetrical cells up to ~99%[23] without evidence of dendrite formation, thus making it one of the best performing electrolytes to date.[27] However, despite these significant developments, the 99.98% benchmark required for commercialization has yet to be achieved.[28] Combinations of salts have also been leveraged to alter the SEI, generally leading to primarily inorganic interphases (LiF presence), reduced interfacial impedance and improved Li metal cycling efficiency.[29–31] Still, the highest plating efficiencies occur with LiFSI as the primary salt, which even exceeds LiPF$_6$ and LiAsF$_6$ in carbonate solvents with additives.[27]

Besides performance improvements, the understanding of how the electrolytes affect Li metal nucleation, growth, and fine nanostructure is still limited. *In situ* optical cells widely used in this effort revealed vivid pictures of dendritic and dead Li formation;[32,33]

however, they failed to provide both chemical knowledge and nanoscale resolution. Conventional electron microscopy can achieve both of these goals, but the beam sensitivity of Li metal introduces significant artifacts. Thus, developing a more comprehensive and accurate tool for accurately characterizing Li metal morphology with minimum sample damage is as equally important as finding a Li–metal compatible electrolyte. Cryogenic (cryo) techniques, which have been widely utilized in the study of biomaterials introduced this capability.[34–36] Recently, our team at UCSD reported one of the initial demonstrations of the power of cryogenic transmission electron microscopy (cryo-TEM) in revealing the nanostructure of deposited Li metal while minimizing beam damage.[37–39] This capability was also extended to focused ion beam scanning electron microscopy (cryo-FIB SEM). Both techniques are leveraged in the present work to investigate the density and morphology of electrochemically plated Li metal at different length scales and as a function of electrolyte composition.

Finally, while it is already a colossal challenge to develop electrolytes that enable efficient plating/stripping of Li, maximizing the energy density of next generation lithium metal batteries will require a cathode with a voltage window beyond the oxidative stability of previously published ether-based systems.[40,41] Very recently, a bisalt-DME electrolyte (2 M LiTFSI + 2 M LiDFOB) enabled reversible cycling of NMC111 at 4.3 V.[42] Despite this remarkable breakthrough, in order to further increase the achievable energy density of batteries, significant advances are still needed to fully access the capacity of Ni-rich NMC cathodes at higher upper cutoff voltages. In this effort, we formulated an electrolyte to achieve these aggressive performance goals. By coupling LiFSI with LiTFSI at high concentrations in DME, we leveraged an expanded stability window to cycle the far more aggressive LiNi$_{0.6}$Mn$_{0.2}$Co$_{0.2}$O$_2$ (NMC-622) in both half cell and "anode-free" (NMC622 *vs.* Cu) cell configurations up to 4.4 V. Herein, we provide a comprehensive picture of the performance improvements garnered by this specific bisalt approach and detail the molecular scale mechanisms responsible for this enhancement.

2. Results and discussion

2.1. Transport and solvation in bulk

The temperature dependence of the bulk conductivity for the bisalt ether electrolyte ("BSEE", 4.6 m LiFSI + 2.3 m LiTFSI in DME), the concentrated single salt ether electrolyte ("SSEE", 4.6 m LiFSI–DME), and a carbonate baseline ("Gen II", 1.0 m LiPF$_6$ EC/EMC 3 : 7) are shown in Fig. 1 along with a few additional compositions for comparison. The discontinuous drop in κ for the LiFSI–DME electrolytes occurs as a result of precipitation of a component from the electrolyte, resulting in a decrease in bulk conductivity and limiting the useful temperature range. In the presence of LiTFSI, LiFSI precipitation is prevented, yielding comparable low temperature conductivities for BSEE and SSEE. The molality (m) to molarity (M) conversions are shown in Table S1 (ESI†).

In addition, conductivity values from molecular dynamics (MD) are also plotted in Fig. 1 as yellow stars for BSEE. An excellent
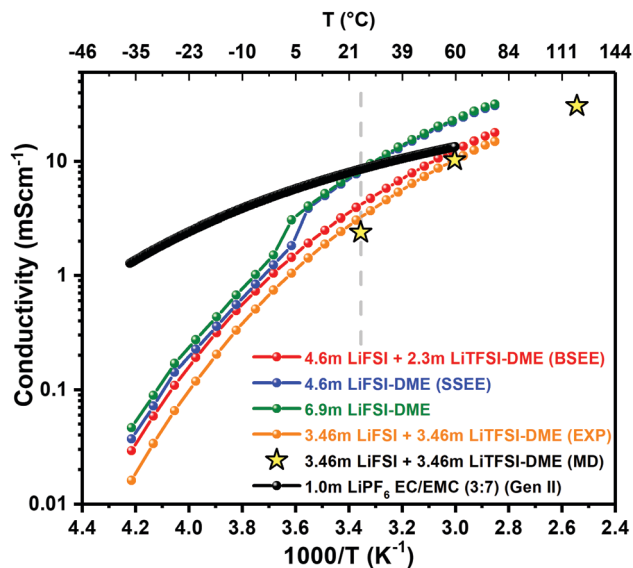
Fig. 1 Conductivity of various single and bisalt ether electrolytes. For comparison, Yellow stars represent conductivity values predicted with molecular dynamics for an equimolal, high concentration bisalt-ether electrolyte.

Fig. 2 Galvanostatic cycling performance of lithium *vs.* copper cells cycled in different electrolytes at a rate of 0.5 mA cm^{-2} to a capacity of 0.5 mA h cm^{-2}.

agreement between MD predictions and experiments is observed, indicating high fidelity of the modeling predictions. Further analysis of MD simulations trajectories showed that DME, Li$^+$ and FSI$^-$ have comparable self-diffusion coefficients, with the TFSI$^-$ self-diffusion coefficient being slightly slower (see Table S2, ESI†), resulting in t_{Li} in the range of 0.51–0.54 depending on temperature. Note that t_{Li} was estimated from ion self-diffusion coefficients assuming that ion motion is uncorrelated. Similar t_{Li} 0.52 and 0.61 were reported from NMR measurements for triglyme(LiFSI) and triglyme(LiTFSI) equimolar mixtures respectively,[43] as well as a t_{Li} of 0.54 for DME : LiTFSI (11 : 8) encapsulated in an organic framework.[44] Impedance spectroscopy yielded lower t_{Li} compared to the NMR-based data indicating inclusion of ion correlation in analysis.[45] Analysis of the Li$^+$ solvate structure from MD simulations yielded that the Li$^+$ cation is preferentially coordinated by TFSI$^-$ over FSI$^-$ with each Li$^+$ being coordinated by 1.14 oxygens from TFSI$^-$ and only 0.93 oxygens from FSI$^-$ anions. Similar preference for the Li-TFSI coordination was also observed in ionic liquids,[46] and is expected to be general and reflected in the chemistries of both the SEI and cathode electrolyte interphase (CEI).

2.2. Li–Cu half cells

The galvanostatic Li cycling efficiency was evaluated in various electrolytes using Li *vs.* Cu coin cells (Fig. 2). The cells were cycled under relatively modest conditions[28] (0.5 mA cm^{-2} to an areal capacity of 0.5 mA h cm^{-2}) with the intent of simultaneously gauging both chemical and electrochemical stability over long term cycling. Under these conditions, the carbonate-based electrolyte had a first cycle efficiency of 54.7%, which increased to 80.0% until the 85th cycle, at which point both the capacity and reversibility significantly decreased due to the
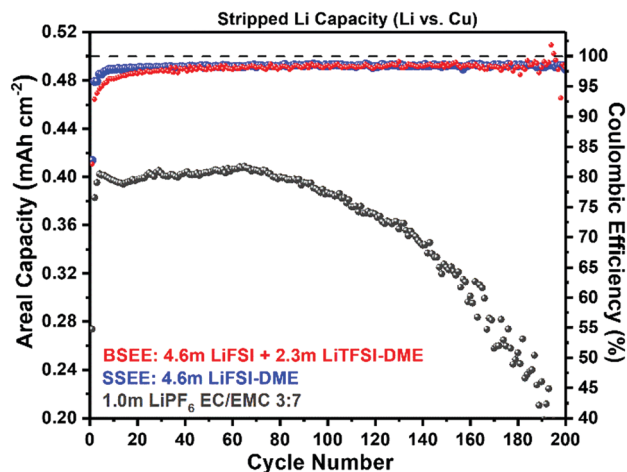
intrinsic instability of carbonates with lithium metal.[47,48] Conversely, the ether-based electrolytes exhibited significantly higher initial efficiencies, which continued to improve in subsequent cycles. In general agreement with the literature, the SSEE quickly reached a high average CE of 98.2% and maintained stable cycling for 200 cycles.[27] The BSEE took slightly longer to reach its peak efficiency, which averaged out to a slightly lower value of 97.9% (Table S3, ESI†). The cause of the slightly slower equilibration along with its underlying benefits will be discussed in detail.

Due to the extreme chemical/electrochemical reactivity of Li metal, the morphology and packing density of plated Li are key factors that dictate cell efficiency and lifetime because they define the true surface area of the reactive Li–electrolyte interface. Some insight regarding the effects of certain cycling parameters (primarily the cycled Li capacity and current density) on growth morphology has been established,[28] but the influence of electrolyte composition and the underlying mechanisms for interphase formation and maintenance still generally remain to be understood. Despite limited understanding, the electrolyte impact is obvious. Fig. 3a–c, shows SEM surface images of Li after the first plating and the tremendous effect of electrolyte on surface morphology and packing density. The carbonate baseline electrolyte produces a mesoporous, highly branched lithium network even after the first plating step, which is consistent with previous results.[21,49] In contrast, both highly concentrated ether electrolytes (Fig. 3b and c) present a microporous, closely packed nodular Li metal morphology, similar to what was shown by Qian *et al.* for 4.0 M LiFSI–DME.[27,41] However, these images only represent the morphology and packing density at the surface. For a more complete perspective, cross sections of the plated films were generated with a cryogenic focused ion beam (cryo-FIB), which overcomes the sensitivity and artifact issues of traditional sample cross sectioning by freezing the Li–metal samples at −170 °C during processing, minimizing surface damage and

782 | *Energy Environ. Sci.*, 2019, **12**, 780–794

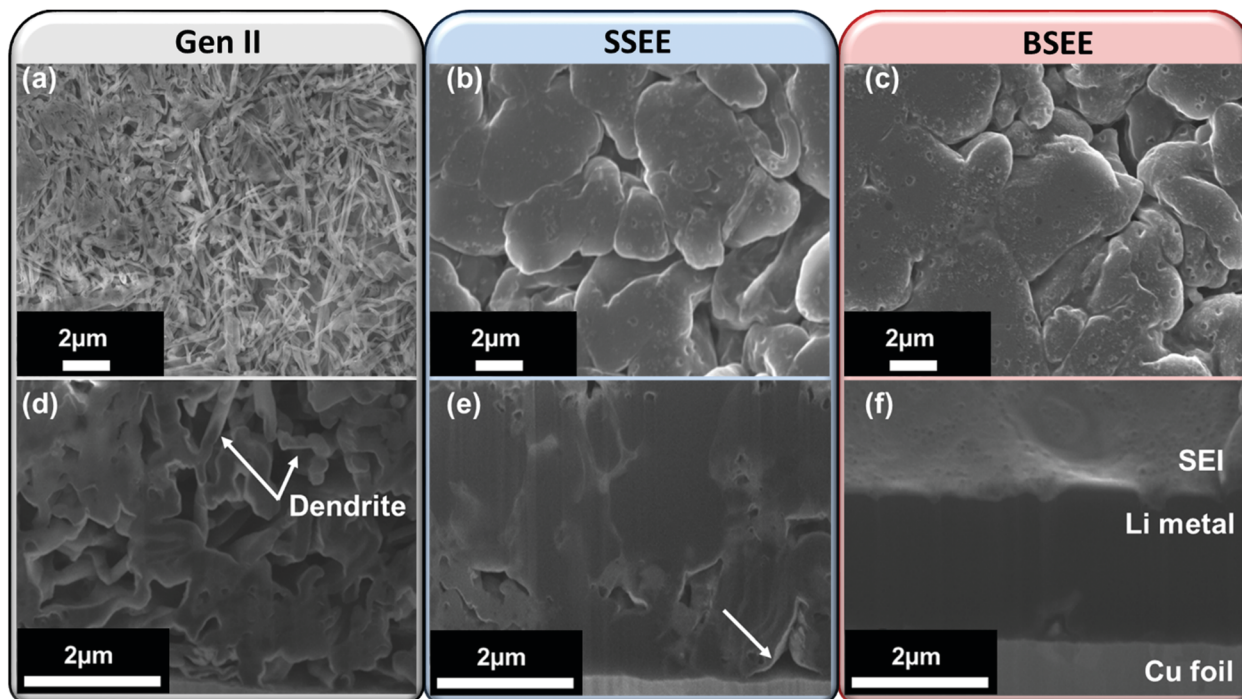This journal is © The Royal Society of Chemistry 2019

Fig. 3   Top view SEM images of the initial morphology of plated lithium and their corresponding Cryo-FIB cross sectional cuts when cycled in (a and d) Gen II, 1.0 m LiPF$_6$ EC : EMC (3 : 7), (b and e) SSEE, and BSEE (c and f).

re-deposition of beam sensitive materials. This method also avoids mechanical deformation associated with "cutting" methods (*i.e.* microtome, scissors, *etc.*), thereby obtaining a more accurate representation of the bulk film. For the lithium plated with the carbonate baseline, the film has a continuous, highly porous network with Li metal branching highlighted by the white arrows (Fig. 3d). Significant void spaces between the Li metal and the Cu foil propagate throughout the film, which has a layer thickness of ∼5 μm and suggests significant inhomogeneities in the areal current density distribution. For the SSEE, the porosity in deposited Li is reduced, with no observable dendritic Li; however, small pores are present close to the Cu interface, as highlighted by a white arrow (Fig. 3e). Nonetheless, the high salt concentration as well as ether solvent increase the Li metal packing density with an average layer thickness of ∼4 μm. Interestingly, despite noticeable positive effects of high salt concentration up to 4.6 m, further increasing the concentration to 6.9 m does not mitigate these issues (Fig. S2, ESI†). This presents an important exception to many recent successful applications of high concentration LiFSI electrolytes and casts doubt over the notion that performance may scale with concentration alone. In contrast, the lithium film plated with the BSEE (Fig. 3f) exhibits a drastic improvement in both film density and reduced plated layer thickness (only ∼2.5 μm). Clearly, some factor(s) surrounding the interplay between LiFSI and LiTFSI generates more uniform Li nucleation and deposition, particularly at the Li–Cu interface. Recently, we have confirmed and further explored this effect with Cryo-FIB tomography.[50] One final note is the similarity between the surface images for the two ether electrolytes (Fig. 3b and c),

which strongly demonstrates the importance of cryogenic cross-section analysis in developing a more comprehensive picture of lithium cycling efficiency despite highly similar surficial appearance.

2.3.   Nucleation growth investigation by Cryo-TEM

Cryogenic TEM (cryo-TEM) was recently used to directly visualize the Li deposition and its amorphous characteristics as well as crystalline growth mechanism in various electrolytes.[37,38] Here, we utilized this new technique to further understand the nucleation and growth of Li metal in each electrolyte. When Li metal is deposited in carbonate baseline, the low magnification TEM image (Fig. 4a) shows the formation of ribbon-like Li metal growing from the TEM grid, as demonstrated by Liu *et al.*[51] The high resolution image (Fig. 4d) shows the crystalline structure of the ribbon. The random Li growth leads to large voids during Li metal deposition and is attributed to low CE in the cell, as demonstrated by cryo-FIB. Conversely, the Li deposited using SSEE (Fig. 4b and e) has a mixed morphology that is dominated by nanosheets and ribbons of Li. After 20 min of deposition the sheets consist of combination of crystalline and amorphous Li, where the nanosheets are more likely to be amorphous, which correspond predominantly to (110), (200), and (211) facets (Fig. S3, ESI†). Remarkably, the use of BSEE (Fig. 4c and f) achieves a significantly more homogeneous nucleation of Li metal on the grid with a nanosheet morphology throughout. High resolution imaging indicates that the deposited Li is in the (110) crystalline orientation with crystalline Li$_2$O present in the SEI. The presence of LiOH in Fig. 4d is an indication of possible reaction between
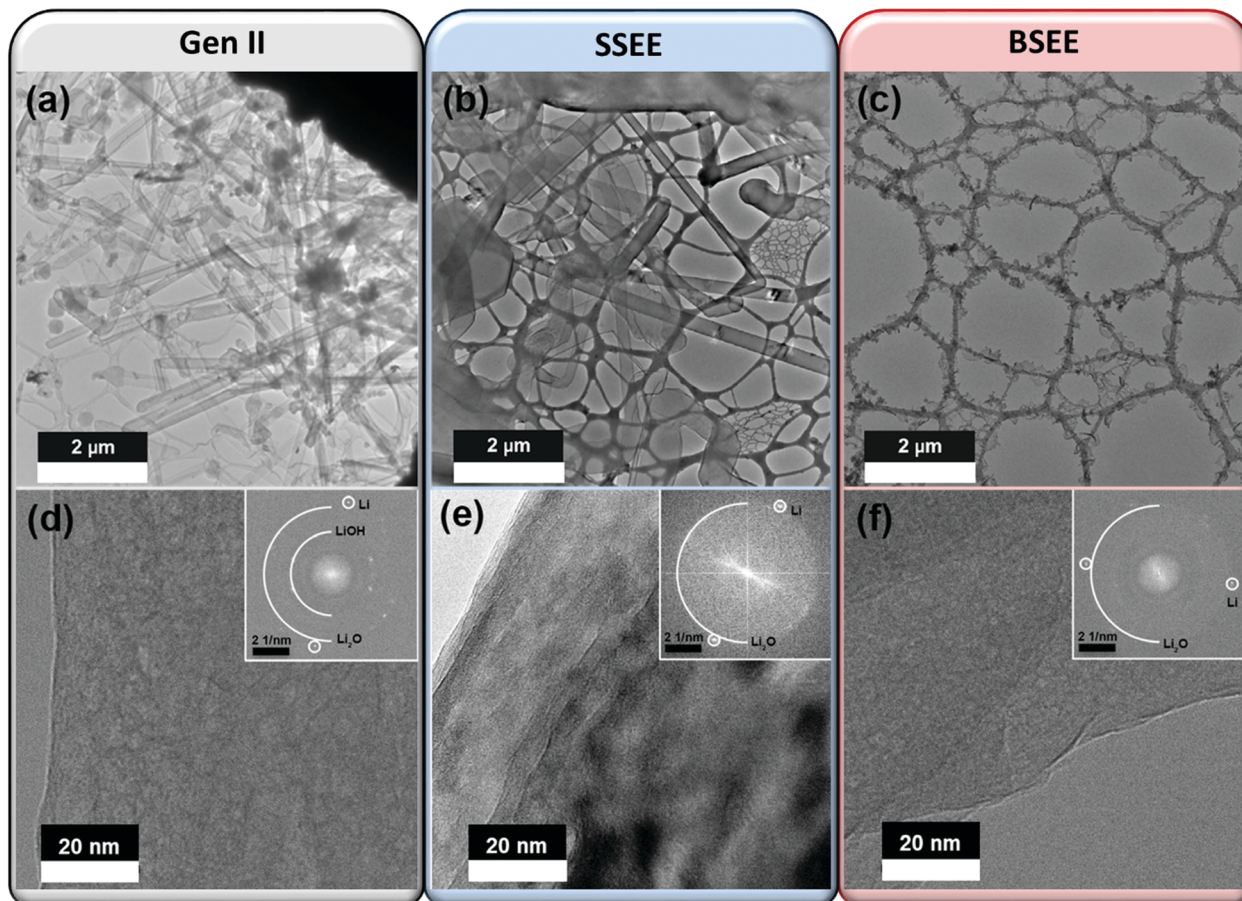
This journal is © The Royal Society of Chemistry 2019

Energy Environ. Sci., 2019, **12**, 780–794 | 783

Fig. 4 Cryo-TEM images of deposited Li using (a and d) 1.0 m LiPF$_6$ EC/EMC (Gen II) (b and e) 4.6 m LiFSI–DME (SSEE) (c and f) 4.6 m LiFSI + 2.3 m LiTFSI–DME (BSEE) electrolyte after 20 minutes of deposition at 0.5 mA cm^{-2}.

Li$_2$O and the carbonate solvents or trace moisture present in the electrolyte. LiF was also detected in some of the ~50 images taken for each electrolyte (Fig. S4, ESI†), but its low intensity and sporadic detection suggest it is a minority SEI component under these conditions. Although this is not demonstrated in our previous work,[38] it gives an indication that time and current density have a significant impact on the chemistry and distribution of SEI components.

2.4. Anode SEI chemistry (XPS)

The SEI generated in both carbonate electrolyte and 4 M LiFSI–DME electrolyte have been extensively studied by various spectroscopic techniques together with computational methods;[20,52,53] however, the addition of LiTFSI changes the interphasial behavior and introduces a new chemistry from the competitive decomposition of these two anions. Interestingly, after the first deposition, the initial formation of sulfide (S^{2-}, ~160 eV) and Li$_2$O (~528 eV) moieties is evident in the SSEE but not present in BSEE (Fig. 5). We attribute this effect to the rapid and extensive reduction of LiFSI and its fragmentation in SSEE (Table S4, ESI†), which becomes kinetically suppressed in the presence of LiTFSI (BSEE) due to slightly stronger interaction between TFSI$^-$ and Li$^+$, its preferential proximity in the double layer to the interface, and steric effects due to the bulkier TFSI$^-$ anion and its partially

reduced fragments.[54] This effect still persists after 200 cycles, with emergence of considerable populations of both lithium oxide/sulfides in both ether electrolytes, but with significantly lower fractions of these terminal reduction products (Li$_2$S, S–S/Li$_2$O) in BSEE as compared with SSEE (Table S4, ESI†). Notably, the initial absence of Li$_2$O in the BSEE-originated SEI presents an incongruity with the Li$_2$O electron diffraction signal observed in cryo-TEM (Fig. 4f). We attribute this difference to the poor depth resolution of XPS (~10 nm) in resolving the Li-SEI layer, particularly as larger areal capacities are deposited and the SEI film thickness increases. The fluorine peaks associated with the LiFSI and LiTFSI decomposition are found at 688.8 eV for CF$_3$ and 687.8 eV for compounds containing S–F, as shown in Fig. S5B (ESI†), which is consistent with previous reports.[23,30] LiF (~685 eV) is also present in SEIs generated from all electrolytes, as corroborated by electron diffraction during cryo-TEM measurements (Fig. S4, ESI†). Fig. S6 (ESI†) compares the fluorine region scans after the first deposition and at the 200th cycle. In the first deposition, the BSEE forms an SEI that is dominated by LiTFSI decomposition, showing the C–F bond with the highest peak intensity with more minor complements of LiF and S–F. In contrast, the SSEE SEI exclusively shows peak signatures of LiF and S–F, which are its primary decomposition products. Interestingly, after 200 cycles the LiF peak intensity increases while the C–F peak intensity decreases for
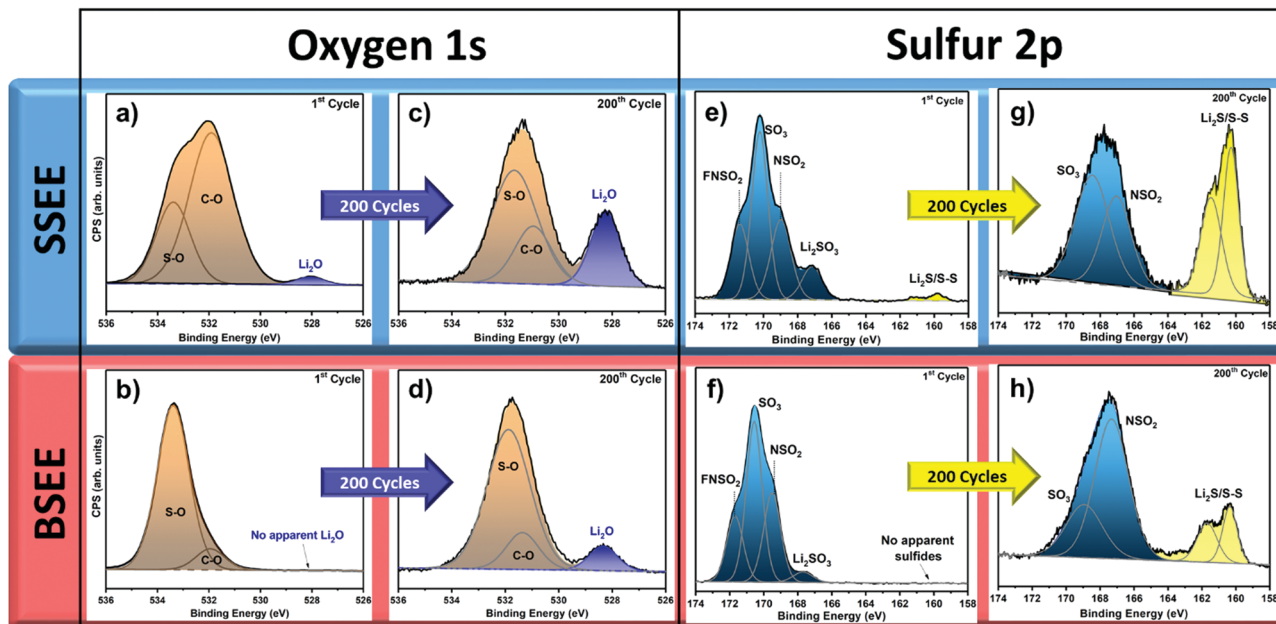
784 | *Energy Environ. Sci.*, 2019, **12**, 780–794

This journal is © The Royal Society of Chemistry 2019

Fig. 5 Region scans of Oxygen 1s (a–d) and Sulfur 2p (e–h) on plated lithium metal after the first deposition (SSEE: a and b; BSEE: e and f) and the 200th deposition (SSEE: c and d; BSEE: g and h).

both ether electrolytes. This suggests that as surface reduction reactions progress during cycling, larger anion fragments such as the C–F moiety are further reduced, ultimately leading to LiF formation. The specific pathways for these reactions are explored in more detail in the next section.

2.5. Modeling predictions for anion reactions on Li|LiF surface

Previous modeling studies have considered the reactivity of DME with LiFSI or LiTFSI salts in direct contact with an unprotected metal surface.[54–58] The metal surface is an electron rich environment, so rapid reduction and decomposition of all electrolyte components (DME, LiTFSI and LiFSI) was observed, albeit at different rates. The onset of anion decomposition was observed at 50–200 fs *via* S–F, S–N, or C–S cleavage. The more reactive LiFSI decomposition can be followed to its end in *ab initio* DFT simulations within 10 ps trajectory, while LiTFSI tends to form larger fragments that survive to at least 40 ps.[54,58] DME decomposition is not observed within such short time-scales with anions present, but simulations of the pure solvent have been shown previously to decompose *via* a 4-electron transfer in an electron-rich environment (approximately 0.9 excess electrons per molecule).[55]

Because it is clear from the previous simulations and experimental evidence that all electrolyte components quickly reduce on bare lithium metal, we take the next step and focus on the modeling of electrolyte reduction and decomposition reactions on the lithium covered with an initial SEI layer. DFT studies of electrolyte reduction at the lithium covered with SEI are extremely challenging and computationally demanding. Previous studies have focused on carbonate-based SEI with electrolyte containing one Li^+ and no counterions.[59,60]

We extend these recent efforts to highly concentrated BSEE. We have chosen LiF, which is less prone to electron leakage compared to Li_2O as a model SEI.[61] This choice is also consistent with LiF being one of the major SEI components for BSEE (see Fig. S6, ESI†).

Specifically, *ab initio* MD simulations were performed at 393 K on a bisalt DME electrolyte (LiFSI + LiTFSI in 1 : 1 ratio, 3.46 m of each salt) in contact with a Li metal anode slab covered by three layers of LiF on both ends as shown in Fig. 6 and Fig. S12, S14 (ESI†). A tri-layer LiF SEI with thickness 4 Å provides about 20–25% of that necessary for passivation.[62] However, even such a thin LiF coating provides some insulation as only the first layer populates any states at the metal E_F.[62] Statistically decoupled electrolyte configurations of LiF – BSEE were generated at 9 ns intervals from force field-based MD also at 333 K. The interval was chosen as it is about 3 times that of the LiTFSI residence time (LiFSI is about 1.4 ns) at 333 K. Additional calculation details are given in Sections 5.1 and 5.2.

A summary of all the observed reactions and the approximate time at which they occurred is provided in Table 1. The final snapshot from 4 of the 7 trajectories taken at the 12 ps mark is shown in Fig. 6. We emphasize the importance of investigating a representative number of the SEI – BSEE initial configurations to avoid drawing conclusions from one or two reactions that occur but might not be representative.

The reacted species from BOMD simulations are highlighted as ball and stick models with solvent and unreacted material as wireframe in Fig. 6. Examination of reaction timescales shown in Table 1 indicates that the most commonly observed reactions are reduction and decomposition of LiFSI *via* S–F or S–N followed by LiTFSI decomposition *via* S–N bond breaking. The cleavage of the C–S bond reported by others
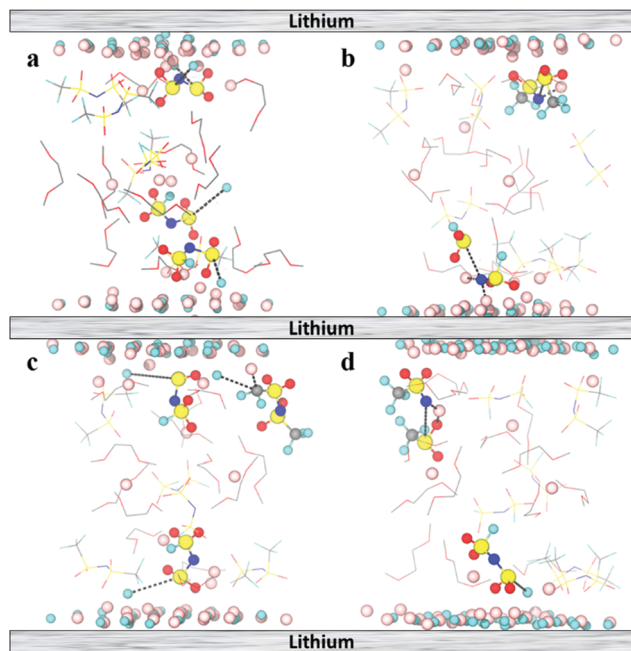
Fig. 6 (a–d) The final snapshots extracted from BOMD simulations of BSEE electrolyte sandwiched between LiF covered Li metal. Four of seven trajectories at 12 ps are shown indicating a tendency for anions to decompose through defluorination or S–N cleavage. Unreacted material is depicted as wireframe with hydrogens excluded. Color scheme: Li (pink), F (cyan), O (red), S (yellow), N (dark blue), and C (grey). Broken bonds are highlighted with a dashed line.

Table 1 Catalog of reactions and the approximate time they occurred for each of the trajectories. '2nd S–F' means the second fluorine from a single FSI^- anion

Run	Species	Time (ps)	Reaction	Broken bond
1	FSI^-	0.18–0.2	$Li + FSI \rightarrow LiF + NS_2O_4F$	S–F
		0.2–0.225	$Li + FSI \rightarrow LiF + NS_2O_4F$	S–F
		3.65	$Li + FSI \rightarrow LiF + NS_2O_4F$	S–F
		8.10	$Li + NS_2O_4F \rightarrow LiF + NS_2O_4$	2nd S–F
2	FSI^-	0.125	$Li + FSI \rightarrow LiF + NS_2O_4F$	S–F
		0.44	$Li + FSI \rightarrow LiF + NS_2O_4F$	S–F
		8.75	$Li + NS_2O_4F \rightarrow LiF + NS_2O_4$	2nd S–F
	$TFSI^-$	4.30	$Li + TFSI \rightarrow SO_2CF_3 + LiNSO_2CF_3$	S–N
3	FSI^-	1.05	$Li + FSI \rightarrow LiF + NS_2O_4F$	S–F
		7.9	$Li + FSI \rightarrow LiF + NS_2O_4F$	S–F
	$TFSI^-$	0.165	$Li + TFSI \rightarrow SO_2CF_3 + LiNSO_2CF_3$	S–N
		0.24	$Li + TFSI \rightarrow SO_2CF_3 + LiNSO_2CF_3$	S–N
4	FSI^-	0.4	$Li + FSI \rightarrow SO_2F + LiNSO_2F$	S–N
	$TFSI^-$	1.7	$Li + TFSI \rightarrow SO_2CF_3 + LiNSO_2CF_3$	S–N
5	FSI^-	0.125	$Li + FSI \rightarrow LiF + NS_2O_4F$	S–F
		1.3	$Li + FSI \rightarrow SO_2F + LiNSO_2F$	S–N
6	FSI^-	0.125	$Li + FSI \rightarrow LiF + NS_2O_4F$	S–F
		0.75	$Li + FSI \rightarrow LiF + NS_2O_4F$	S–F
	$TFSI^-$	10.5	$Li + TFSI \rightarrow LiF + F_2CSO_2NSO_2CF_3$	C–F
7	FSI^-	0.125	$Li + FSI \rightarrow LiF + NS_2O_4F$	S–F
	$TFSI^-$	0.71	$Li + TFSI \rightarrow SO_2CF_3 + LiNSO_2CF_3$	S–N

was not observed in our BOMD simulations.[58,63] In a single trajectory, C–F cleavage in $TFSI^-$ was observed at 10.5 ps. This demonstrates that $TFSI^-$ can serve as a F-donor on a longer timescale than FSI^- and is consistent with Markevich *et al.*,[63]

Piper *et al.*,[64] and the observation of CF_2 from XPS. The initial decomposition reactions occur in our BOMD simulations on comparable timescales, within the first few hundred femtoseconds. However, there is a significant delay in subsequent reactions, indicating emergence of an insulating double layer evolving on the LiF (see Fig. S14, ESI†). Leung and coworkers have shown that surface dipoles can affect electrolyte decomposition kinetics.[64] In the present study, the double layer mimics a thicker SEI that delays follow-up reactions and promotes inorganic SEI-formation.

Despite the emergence of a passivating electric double layer, modeling predicts that the slowly reacting $TFSI^-$ plays a role in controlling the kinetics of FSI^- decomposition through absorbing electrons from the metal and in displacing a fraction of the FSI^- from the surface. Slower reaction rates increase the timescale for LiF and other LiFSI reduction products to aggregate and form a more uniform and robust SEI as opposed to rapid and excessive LiFSI reduction and saturation of bulk electrolyte with reduction products. We did not observe DME decomposition in BOMD simulations, supporting XPS conclusions that salt contributes to the majority of the later SEI formation reactions. The lower reduction potential of DME relative to the anions generally prevents solvent decomposition reactions on the bare metal electrode.[55,65] Viscosity of the bisalt electrolyte relative to the single salt variant may also play a role in slowing degradation as well. Molecules and fragments experience drag due to interaction with the surface and could provide a lingering screening effect. Self-diffusion coefficients of surviving $TFSI^-$ near the Li|LiF surface averaged to 2.25×10^{-7} cm^2 s^{-1} at 120 °C, more than an order of magnitude reduced from $TFSI^-$ in pure DME at near-ambient conditions.[66]

2.6. Anodic stability of ether-based electrolytes

In order to evaluate the effect of the bisalt composition on oxidative stability, we measured linear sweep voltammograms (LSV) using a Pt *vs.* Li cell (Fig. 7a). Consistent with Qian and coworkers, we observe at ~4.4 V the onset of the oxidation current for SSEE.[27] The higher salt concentration bisalt electrolyte pushed the oxidation onset threshold (0.1 mA cm^{-2}) to ~5 V, which is even higher than the carbonate baseline (4.8 V). A discussion of other recent and related measurements of oxidative stability of ether-based electrolytes can be found in the supporting information. We attribute this increase to essential elimination of free DME solvent in BSEE. MD simulations predicted the BSEE which has a total salt concentration of 6.9 m has only 1.8% of DME ether oxygens that are not coordinated by the Li^+ cation within 2.8 Å, suggesting that there are virtually no free DME solvent molecules. Previous MD simulations of highly concentrated electrode–electrolyte interfaces have also indicated that at the positive electrode, $TFSI^-$ anions occupy most of the inner-Helmholtz layer, forcing the solvent away from the electrode surface and screening it from oxidizing potentials at the electrode surface.[67] While our data do not allow us to directly decouple relative contributions from these two mechanisms responsible for enhanced oxidative stability,

786 | *Energy Environ. Sci.*, 2019, **12**, 780–794

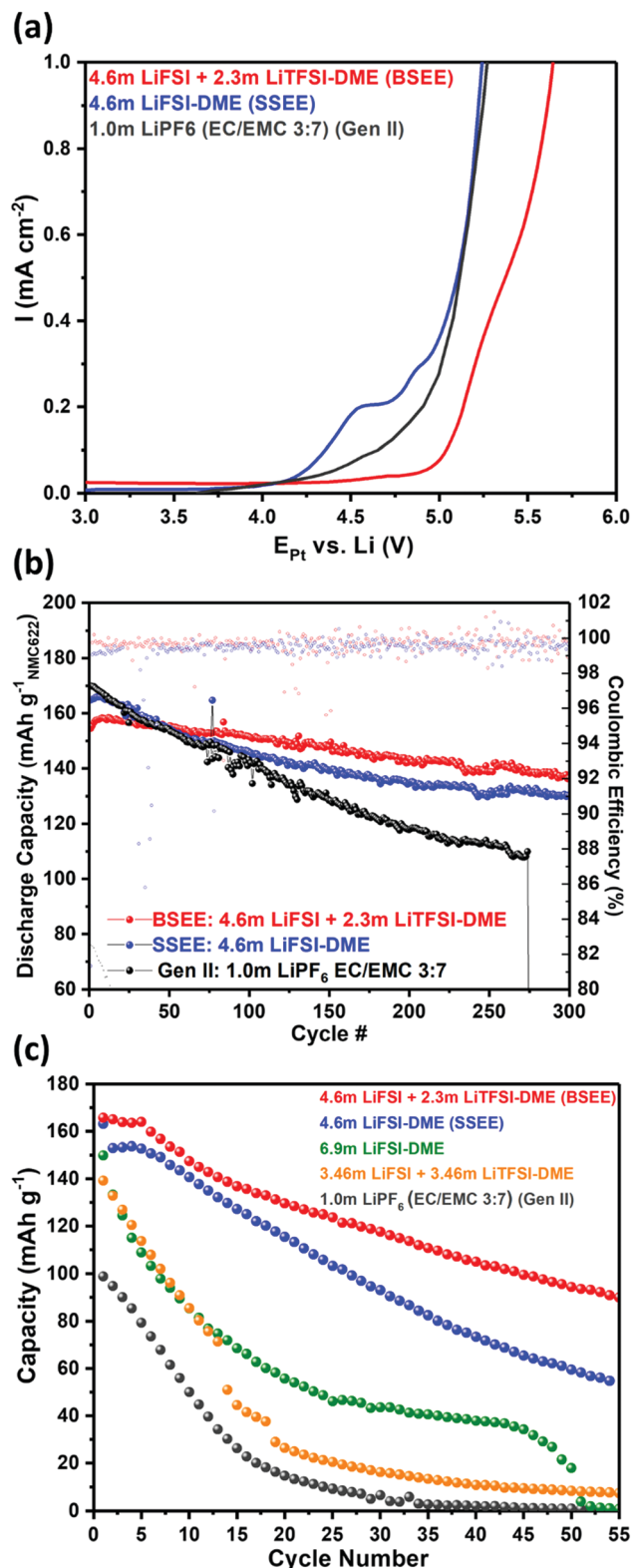This journal is © The Royal Society of Chemistry 2019

Fig. 7 Electrochemical testing in various cell configurations: (a) positive LSV sweep to gauge anodic stability of electrolytes (b) NMC622 vs. Li in Swagelok cells, and (c) NMC622 vs. Cu cells.

similar effects have also been observed in concentrated aqueous electrolytes.[68,69]

2.7. NMC622 half cell and "anode free" cell testing

Previous cell testing for ether-based electrolytes was generally limited to lithium air, lithium sulfur, and other cathode chemistries with relatively low redox potentials such as lithium iron phosphate (LFP).[23,70] Qian and coworkers determined that (LiFSI–DME) has an anodic stability of >4.4 V regardless of concentration, making it a suitable electrolyte for a wider range of chemistries, but these electrolytes were only tested on LFP in half and anode free cell configurations.[27,41] Encouraged by the promising oxidative stability displayed on Pt, we applied BSEE directly to a very challenging chemistry that even carbonate-based electrolytes cannot fully support. We galvanostatically cycled NMC622 Swagelok-type half cells at C/3 to an upper cutoff voltage of 4.4 V—a previously untouchable limit for ether-based systems, especially with Ni-rich electrodes. The cells with BSEE achieved a capacity retention of >88% of its original capacity after 300 cycles—an enhancement of ~10% over the SSEE and >25% over the carbonate baseline (Fig. 7b). A similar comparison of these electrolytes in capacity *versus* time provides a better perspective of chemical stability (Fig. S9, ESI†), showing that BSEE can cycle continuously beyond 1400 hours (~2 months) with >88% capacity retention in a high nickel content NMC half-cell cycled to high voltage (4.4 V).

Half cell configurations containing a huge excess of lithium can introduce significant ambiguity into accurately gauging cycling efficiency since parasitic side reactions can be camouflaged by an essentially "infinite" reservoir of lithium. In addition, maximizing energy density for commercial cells requires minimization of all non-active material mass contributions in the cell. To rigorously confirm performance in light of these considerations, Qian and coworkers introduced the "Anode-Free (AF)" cell configuration, originally consisting of LFP vs. Cu, in which the lithiated cathode provides a finite source of lithium in the cell.[41] Repeated deposition and stripping in this manner presents the true reversibility of the electrolyte due to a fixed capacity of lithium in the cell.[71] In this work, AF cells with NMC-622 were used to test all electrolytes (Fig. 7c). It is known that the performance of Li metal plating and stripping in AF and half cell configurations improve substantially with variable rate cycling, where the Li metal is plated at a slow rate and stripped at a fast rate.[41,72] Therefore, our AF cells were plated at C/10 and stripped at C/3 to obtain the highest efficiency. The cell cycled with Gen II electrolyte quickly fades with no remaining capacity after 30 cycles, which is consistent with the literature.[27] Meanwhile, BSEE (4.6 m LiFSI + 2.3 m LiTFSI–DME) outperformed SSEE (4.6 m LiFSI–DME) with initial CEs of 80.5% vs. 78.1%, and after 54 cycles, the BSEE cell had a residual capacity of 90.9 mA h g^{-1} and CE of 98.6% as compared to 54.8 mA h g^{-1} and a CE of 97.4% for SSEE (see Table S5, ESI†). We also considered the possibility that the overall capacity and CE improvement over SSEE electrolyte could be solely attributed to the global lithium content or salt concentration within the cells. To test this concentration argument, we assembled AF cells with similar global lithium content to that of the 6.9 m BSEE, including 6.9 m LiFSI DME and 3.46 m LiFSI: 3.46 m LiTFSI–DME. As shown in Fig. 7c, 6.9 m LiFSI DME and 3.46 m LiFSI:

This journal is © The Royal Society of Chemistry 2019

Energy Environ. Sci., 2019, **12**, 780–794 | 787

3.46 m LiTFSI–DME AF cells fade significantly faster than the 6.9 m bisalt electrolyte, which indicates that the LiFSI/LiTFSI ratio plays a vital role in lithium plating morphology, as illustrated by cryo-FIB (Fig. 3 and Fig. S6, ESI†), and the rate and extent of interphasial reactions as supported by our simulations. The capacity fade in AF cell configurations still requires additional work, but these initial results are promising for an aggressive high voltage (4.4 V), high nickel chemistry system with no excess lithium.

The CEIs generated on NMC-622 were also investigated to determine the relation between respective surface chemistries and high voltage cycling performance. Fig. 8a compares the C1s high resolution spectra of all three electrolytes (BSEE, SSEE, and 1.0 m LiPF$_6$ EC/EMC). Because NMC-622 is a composite electrode with a binder, the PVDF peak is present at 292.3 eV in the spectra for all electrolytes. The carbonate baseline shows the expected oxidation components associated with carbonate oxidation (C–O at 285.86 eV, O–C–O at 288.6 eV, CO$_3$ at 290.56 eV).[73,74] Conversely, the CEI generated from the ether-based electrolytes are primarily inorganic, containing products of chemical reduction of the anions or their fragments at catalytic Ni sites (as shown later with DFT), as opposed to the more traditionally expected electrochemical oxidation. The peak at approximately 290 eV, which is present in both SSEE and BSEE, can be associated to the C–N bond that forms as a result of DME reacting with the anion decomposition products in the oxidizing environment as predicted by DFT calculations.[23] We propose that the C-NSO peak is largely due to the LiFSI reduction reaction. The CF$_3$ peak (292.9 eV in Fig. 8a and 688 eV in Fig. 8b) is associated with the reduction of LiTFSI, demonstrating that both anions contribute via reduction processes to the CEI chemistry. The C1s spectra and O1s spectra (Fig. S10, ESI†) suggest the presence of oxidized DME in the CEI; however, the decomposition of DME (C–O) is slightly diminished in BSEE CEI with an atomic percentage of 13.31% compared to

14.78% in SSEE CEI. The higher salt concentration in BSEE supports a more conformal, anion-based CEI, as indicated by decreased atomic percentages (Fig. 8c) carbon-based moieties compared to both Gen II and the SSEE CEI. Moreover, both ether-based electrolytes have less lattice oxygen percentage (BSEE: 1.47% and SSEE: 2.11%) compared to the carbonate based electrolyte (5.59%), suggesting that these highly concentrated electrolytes provide a more uniform CEI which may prevent lattice oxygen exposure.[25] The S2p spectra (Fig. S11, ESI†) further illustrates this point. As noted by Kim et al., LiFSI and LiTFSI have distinct decomposition peaks associated with each salt.[23] Fig. S11 (ESI†) demonstrates that the CEI generated by SSEE primarily has peaks that correspond to SO$_2$ functionalities located at 169.96 eV and 171.3 eV.[75] These peaks are also present in BSEE; however, there are two new peaks: SO$_3$ functionalities located at 167.09 eV and 169.10 eV corresponding to LiTFSI fragments.[76]

2.8. Solvent and anion reactions on Li$_x$NiO$_2$ surface

During charging, organic solvents are susceptible to oxidation on high voltage electrodes including lithium metal oxides (LMO), especially those containing nickel centers.[77–79] Additionally, some anion decomposition products (e.g., LiF and larger fragments) have been found to make up part of the CEI. Here, LiNiO$_2$ (LNO) is used to model a NMC cathode, eliminating concerns about metal center distribution at the surface. We examine both anion and solvent decomposition on the Li$_x$NiO$_2$ surface, where $x = 0.5$ and 1. Only the solvent-to-surface H-transfer and anion defluorination are considered in the present study. Calculation details are outlined in Section 3.3.

The solvent in ultrahigh vacuum conditions was found to adopt a non-planar configuration with each oxygen loosely coordinated to neighboring nickel atoms in the surface (Fig. S15, ESI†). Upon oxidation, H dissociates from the DME structure and binds to a nearby surface oxygen, producing a CH$_2$ radical.

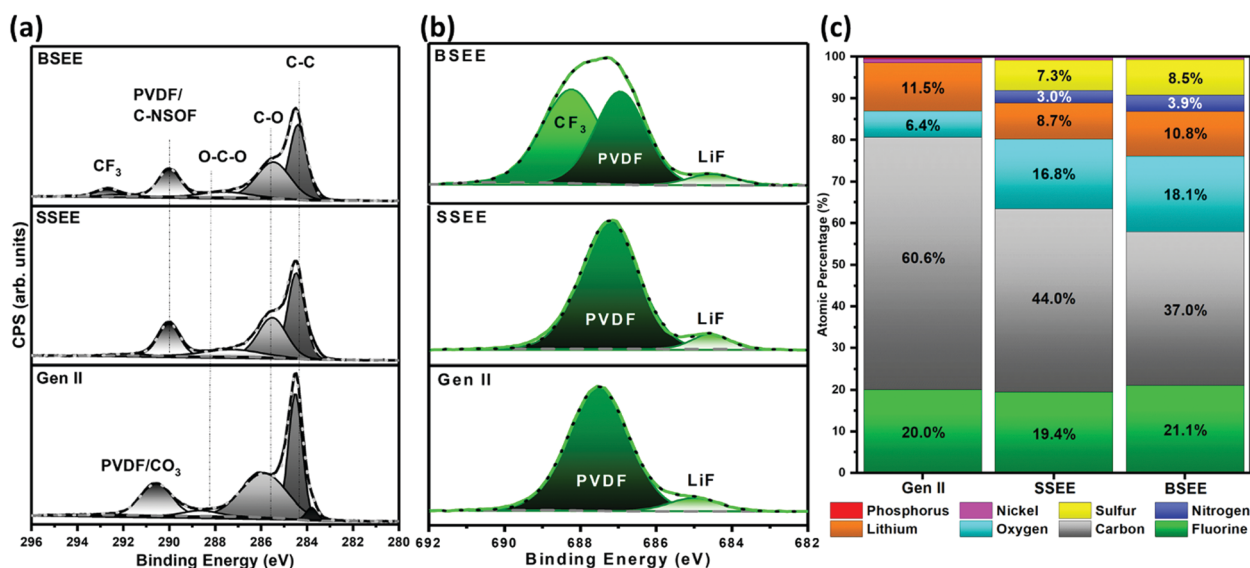Fig. 8 XPS region scans of (a) carbon 1s, (b) fluorine 1s and (c) total elemental percentages based on survey data of cycled NMC622 after 200 cycles.

788 | Energy Environ. Sci., 2019, 12, 780–794

This journal is © The Royal Society of Chemistry 2019

The radical is stable on the $LiNiO_2$ surface, with a reaction energy of -0.24 eV. The radical could not be isolated on the $Li_{0.5}NiO_2$ surface. Chemisorption of the radical through a C–O bond proceeded with a reaction energy of -3.70 eV (-4.02 eV) on $Li_{0.5}NiO_2$ and -2.90 eV on $LiNiO_2$. The two energies for $Li_{0.5}NiO_2$ reflect two observed termination states for the reaction: (1) O–H projected into vacuum and (2) O–H nearly parallel with the surface and Li migrates to an interstitial site. Only state (1) is available to the $LiNiO_2$ structure. The dissociation reaction energy of DME on $LiNiO_2$ is comparable to that of EC from Giordano *et al.*[80]

Next we investigated the origin of the inorganic part of the protective CEI that is critical to achieving high reversibility in these cells.[81,82] Here, DFT calculations on a neat Li_xNiO_2 surface (Fig. 9) are performed to determine how the anions may be expected to contribute to CEI formation at high and low voltages. LiFSI and LiTFSI were both found to have a similar binding motif on the $Li_{0.5}NiO_2$ surface, with O–N–O binding to available Li–Ni–Li sites, respectively. A neutralizing Li^+ was positioned as if it were in the electrolyte, balanced between the non-adsorbed oxygens. The fluorinated moieties were projected nearly parallel to the surface. Modeling the reaction as a two-step process of radical generation and subsequent adsorption, DFT predicts the first step to be rather inaccessible. Direct defluorination *via* oxidation of the anion was found to have reaction energies of 1.37 eV and 2.75 eV for LiFSI and LiTFSI, respectively. The adsorption of the $TFSI_F$ radical pushes the net reaction energy closer to 0 eV, however, the $LiFSI_F$ product decomposes to $NSO_2F + SO_2 + (Ni)F$.

Considering the unviability of the oxidation mechanism at high charge to provide a source of the CEI fragments observed in XPS spectra, DFT calculations were also done for the fully discharged state. An extra Li^0 was added near the surface as an electron source and to support deposition of F^- on a surface Ni. This approach is similar to that discussed by Kim *et al.* on the role of excess surface Li scavenging by anions to promote LiF formation on lithium nickel cobalt aluminum oxide.[83] The first step of the Li_2FSI degradation is similar to that observed on the anode and in cluster calculations.[83] DFT calculations suggest that a 2-electron reaction occurs, where defluorination is supported by formation of LiF on Ni and the elongation of the S–N bond in FSI_F. The resulting fragments are LiF, NSO_2F, and SO_2 with a reaction energy of -0.08 eV (Fig. 9(a and b)). Previous work has shown defluorination of Li_2TFSI coupled with reduction to be a viable mechanism of decomposition.[84] However, the reaction of Li_2TFSI on the cathode surface resulting in radical generation was found to be unfavorable with a reaction energy of $+1.4$ eV (Fig. 9(c and d)). Allowing the radical to quench on the surface was found to be favorable, however, at -2.43 eV relative to the unreacted state. These results suggest FSI^- and fluorinated fragments from FSI^- decomposition may contribute to LiF deposition on the cathode surface, while the LiTFSI decomposition is kinetically hindered. DME and Li_2FSI reactivity with the cathode surface yielding O–H bonds and Ni–F–Li likely facilitates transition metal dissolution from cathodes leading to capacity fade.[85] Drawing from the relative stability of $TFSI^-$ reaction products compared to FSI^-, it may be more likely that $TFSI^-$ contributes to the interfacial stabilization by shielding DME from direct contact with the cathode surface and by CEI formation through diffusion of reduced products from the anode to the cathode surface. This "shuttle", or exchange of material between electrode surfaces has been previously
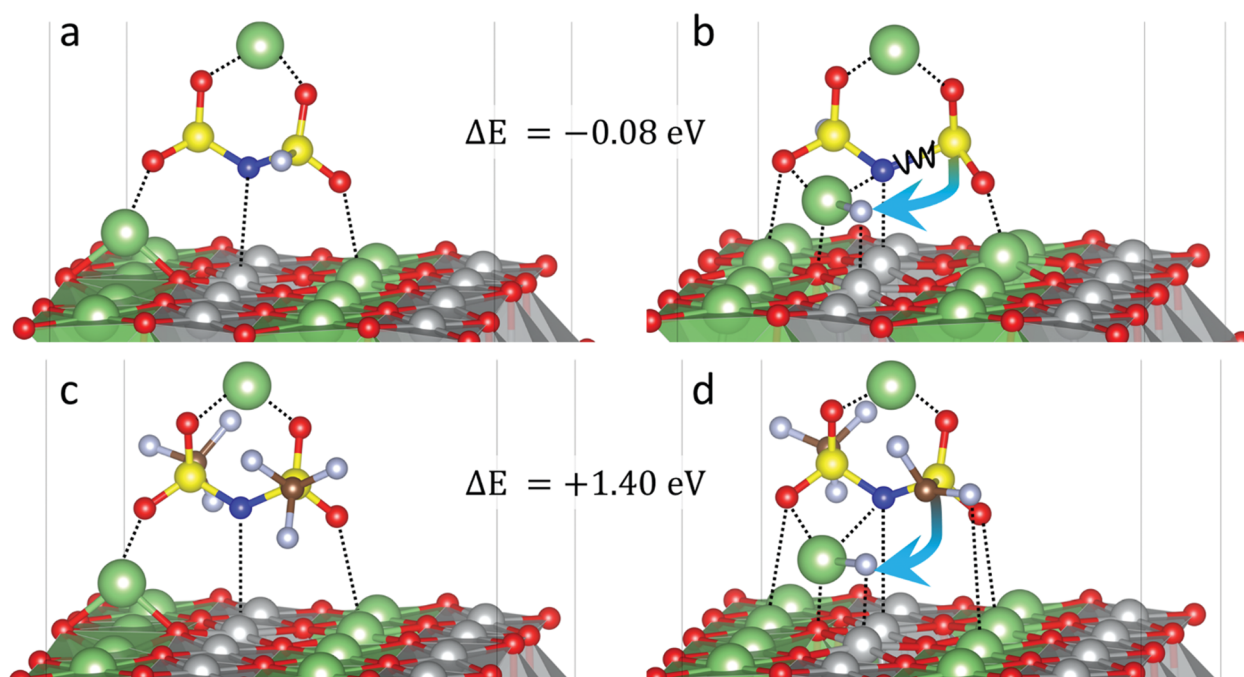

Fig. 9 Reaction mechanism of Li_2FSI and Li_2TFSI on $LiNiO_2$ (1 0 4) surface. Colors: Li (green), S (yellow), O (red), N (blue), Ni (dark grey), F (light grey), C (brown). Initial states (a and c) are shown for LiFSI and LiTFSI, respectively, with arrows indicating the defluorination reaction (b and d).

This journal is © The Royal Society of Chemistry 2019

Energy Environ. Sci., 2019, **12**, 780–794 | 789

confirmed experimentally[86] and was recently examined by Zhang and coworkers with XPS.[82]

3. Conclusion

The bisalt effect on the interphasial chemistries of both Li–metal and high Ni cathode materials like NMC622 was thoroughly investigated *via* both experiments and computation. It was found that the co-existence of two anions (TFSI⁻ and FSI⁻) introduces entirely new interphases *via* preferential decomposition mechanisms. Benefiting from the bisalt effect, plated Li metal adopts a denser, more conformal morphology, while anode-free NMC622 cell configurations showed that global lithium content and salt concentration were not the primary performance-enabler of BSEE electrolyte, but rather a carefully observed interplay between LiFSI and LiTFSI and their reduced anion fragments. In addition, a rudimentary safety analysis (Fig. S16, ESI†) suggests the addition of LiTFSI may offer a pathway towards mitigating known safety risks associated with electrolytes based on concentrated LiFSI and/or ether solvents; however, this result requires rigorous safety testing in actual, large format cells, especially if the intended system includes lithium metal for practical applications. Altogether, a comprehensive investigation coupling experimental and modeling methods provides new insight into key electrolyte decomposition reactions at both negative and positive electrodes. The obtained fundamental understanding addressed a key knowledge gap regarding how the increasingly common addition of a second salt can be leveraged for regulating the timescale, chemistry, and extent of interfacial reactions, promoting efficient plating/deplating of lithium metal, and potentially supporting widespread implementation of high energy density NMC cell configurations with limited or no excess lithium.

4. Experimental section

4.1. Electrolyte preparation

The electrolytes were prepared using Lithium bis(fluorosulfonyl) imide (LiFSI Oakwood Products, Inc.-battery grade (>99%)), lithium (trifluoromethanesulfonyl) imide (LiTFSI Solvay-battery grade), lithium hexafluorophosphate (LiPF$_6$ BASF-battery grade), 1,2 dimethoxyethane (DME, BASF-battery grade), ethylene carbonate (EC, BASF-battery grade), and ethylmethyl carbonate (EMC, BASF-battery grade). All lithium salts were used as received and the solvents were dried using activated molecular sieves for 72 hours prior to making the electrolytes. All electrolyte solvents and solutions were stored and handled in an argon-filled Vacuum Atmospheres Nexus One glovebox with measured levels of O$_2$ and H$_2$O < 1 ppm.

4.2. Electrolyte characterization

4.2.1. Linear sweep voltammetry. A three electrode Swagelok cell containing Li metal as the counter and reference electrode with platinum metal disk (0.5 inch diameter) as the working electrode was used for all LSV measurements. A glass fiber

separator (Whatman QMF) was included to avoid cell shorting, and the cells were filled with 300 uL of electrolyte. The experiments were carried out on a single channel Gamry Potentiostat (Reference 3000), sweeping from OCV to 6 V at 5 mV s⁻¹. Experiments were conducted three times for each electrolyte to ensure reproducibility.

4.2.2. Electrolyte conductivity. Electrolyte conductivity κ of the electrolytes were measured with a Solartron potentiostat at selected temperatures within a Tenney Jr. environmental chamber. The conductivity cells consist of a pair of platinum–iridium electrodes. The cell constants of a nominal value of 0.1 cm⁻¹ were calibrated with a standard KCl solution of 111 mS cm⁻¹ nominal value. The temperature measurements ranged from 60 to −10 °C in 10 degree decrements.

4.3. Electrochemical testing

4.3.1. Lithium *versus* copper. Copper foil was cut into 1/2 inch diameter disks (1.27 cm²) and washed in 1.0 M HCl solution for 10 minutes. The Cu disks were rinsed with deionized water (three times) and acetone (three times), dried under vacuum for 12 h. The washed Cu foil was assembled in the coin cell as the working electrode while the Li metal (0.15 mm thick, FMC Corp) was the reference and counter electrode. Asahi Kasei C5 was used as the separator and soaked in 120 μL of electrolyte. The cells were first discharged until they reached an area capacity of 0.5 mA h cm⁻² and charged until reaching 1.0 V (all at various currents).

4.3.2. Half cell/anode free coin cells. NMC622 electrodes were provided by the CAMP Facility at Argonne National Laboratory. A slurry of 90 wt% NMC622 (ECOPRO NCM040-10A) with 5 wt% Timcal C45 and 5 wt% Solvay 5130 PVDF was deposited on 20 μm thick Al foil with an areal capacity of 1.44 mA h cm⁻². Swagelok two electrode half cells were assembled using 1/2″ diameter anode (Li metal) and cathode (NMC-622) disks. Whatman GF/F separator was used as the separator which contained 70 μL of the desired electrolyte. All half cells were cycled at C/3 for both charge and discharge without a formation cycle in a Maccor battery cycler. For anode-free cells, NMC622 electrodes were punched to 9/16″ diameter (1.6 cm² area) and assembled in 2032 coin cells (Hohsen Corp.) Asahi Kasei C5 was used as the separator and soaked in 70 μL of the desired electrolyte. Cu foil disks (5/8″ diameter) were used as the counter electrode. The anode free cells were cycled at C/10 during charge cycle and C/3 during the discharge state.

4.4. Sample investigation

4.4.1. Scanning electron microscopy (SEM). The deposited Li metal on Cu foil were disassembled and washed with anhydrous DMC in the glovebox. The sample was mounted on the SEM sample holder in the glovebox then imaged using ZEISS Aurgia SEM with an ES2 detector at 5 kV.

4.4.2. XPS sample preparation/analysis. Following cycling, all coin cells were disassembled in an argon-filled Vacuum Atmospheres Nexus One glovebox (H$_2$O < 1 ppm, O$_2$ < 1 ppm). The electrodes were rinsed with anhydrous dimethyl carbonate and dried in vacuum at room temperature to evaporate any residual solvent. The samples were transferred to a PHI

790 | *Energy Environ. Sci.*, 2019, **12**, 780–794

This journal is © The Royal Society of Chemistry 2019

Versaprobe III XPS system using a sealed vacuum transfer capsule enabling rigorous air/moisture exclusion, as to not alter the surface chemistry. The XPS was operated using Al anode source at 15 kV with a 100 μm × 100 μm spot size and charge compensation was provided by the PHI charge neutralization system to eliminate differential charging. Survey scans were collected with a pass energy of 224 eV and a 1.0 eV step size followed by high-resolution scans with a pass energy of 26 eV and a step size of 0.05 eV. Peak fitting was performed using CasaXPS software (version 2.3.15, Casa Software Ltd), using 70/30 Gaussian/Lorentzian line shapes on a linear background. Quantification was performed using peak area corrections to account for the photoionization cross section of each element and the instrument geometry. All spectra were shifted relative to the binding energy of the carbon 1s sp^3 (assigned to 284.5 eV) to compensate for any off-set during the measurement.

4.4.3. Cryo-focused ion beam. The deposited Li metal on Cu foil were disassembled and washed with anhydrous DMC in the glovebox. The samples were mounted on the SEM sample holder in the glovebox then transferred to a FEI Helios Nano-Lab Dualbeam equipped with a CryoMat integrated cryo-stage and air-free quick loader (FEI). At high vacuum ($\sim 10^{-6}$ mbar) the samples were cooled down to $-170\ ^\circ$C and maintained under continuous liquid nitrogen cooling during SEM imaging and FIB operation. Samples were cross-sectional milled at 30 kV and 5 nA ion beam current with 100 ns pixel dwell time and cross-sectional cleaned twice at 0.5 nA and 0.3 nA respectively. SEM images were taken with an ETD detector at 5 kV.

4.4.4. Cryo-transmission electron microscopy. The coin cells were made following a similar protocol to our previous publication.[38] All the Li metals for the cryo-TEM analysis were deposited on the lacey carbon instead of the pure copper grid. On pure Cu grid the Li metal is unstable even under cryo environment and required substrate to support such as the lacey carbon. Micrographs were recorded on a field emission gun (FEG) JEM-2100F Cryo-TEM, equipped with a OneView camera and operated at 200 keV. The Li metal was directly deposited in a lacey carbon grid at 0.5 mA cm^{-2} for 20 min. The TEM samples were loaded onto the cooling holder in a home-made glovebox and transferred to TEM system with continuously Ar flowing. The images were taken at a magnification of 500k× when the temperature of samples reached about 100 K. All the processes avoid any exposure to air and liquid N$_2$, minimizing the potential damage to Li metal.

5. Computational methods

5.1. Polarizable force field-based molecular dynamics simulations

MD simulations were performed on 3.46 m LiTFSI 3.46 m LiFSI in DME using a simulation cell comprised of 308 DME, 96 LiTFSI and 96 LiFSI. Simulations were performed WMI-MD code at 393 K, 333 K and 298 K. Equilibration runs were 22–48.5 ns in *NPT* ensemble followed by production runs in *NVT* ensemble that were 38–69 ns long.

Previously developed LiFSI and LiTFSI force field parameters were used.[25,79] DME charges were refit to reproduce electrostatic potential calculated at MP2/aug-cc-pvTz level, while DME/Li$^+$ repulsion parameters were refit to reproduce DME/Li$^+$ binding energies calculated at G4MP2 level. The Li$^+$/TFSI$^-$ repulsion parameters were transferred to Li$^+$/FSI$^-$. Simulations parameters and addition simulations details are given in ESI.†

MD simulations were also performed for DME doped with LiTFSI and LiFSI sandwiched between LiF surfaces at 333 K in order to generate initial geometries for BOMD simulations investigating electrolyte reduction at the LiF surfaces covering lithium metal. MD simulation box consisted of 13 DME, 4 LiTFSI and 4 LiFSI. Box dimensions were 14.22 Å × 14.22 Å × 24 Å. System was initially for 16 ns. 14 subsequent runs 9 ns each were performed to generate configurations for BOMD simulations.

5.2. *Ab initio* molecular dynamics on Li anode

All anode simulations were done with CP2K 5.1.[87] Initial configurations (7 total) of electrolyte and LiF were prepared from force field simulations described above. The interface dimensions (*xy*) were pre-strained to match those from previous density functional theory (DFT) calculations. Each configuration was optimized at the PBE+D3/DZVP-MOLOPT-SR-GTH level of theory, with a 520 Ry cutoff, 600 K Fermi–Dirac smearing, and 600 total additional molecular orbitals.[88–93] A pre-strained Li metal slab was added to this cell (having the same xy dimensions as the LiF/electrolyte cell). The (0 0 1) surfaces of each material were joined. Visualizations were prepared in VESTA and VMD 1.9.3.[94,95]

A cell optimization at 1 ± 10 bar was performed on the final assembly, with all other theoretical considerations the same as previously reported. For these optimizations, the electrolyte coordinates were frozen to prevent decomposition (which otherwise always occurred). The only interactions not fully coupled in this process are those of the electrolyte in the presence of Li metal. Spin-polarization is considered where electrolyte decomposition is possible. Lattice parameters were in the following ranges 14.1–14.2 Å by 14.1–14.2 Å by 44.9–46.5 Å.

Some 12 ps of constant volume (*NVT*) dynamics was carried out for each of the configurations with initially preserved electrolyte. A somewhat elevated temperature of 393 K was used in conjunction with tritium masses (for a 1 fs timestep) to balance the cost of adding spin-polarization into such large systems. Simulations were thermostatted with the adaptive Langevin thermostat and a 10 fs coupling constant.[96] Runs were done in installments of 3 ps each. Electrostatic potentials were computed with PBE at every 25th configuration.[88] Potentials were averaged over times with 0, 1, 2, *etc.* reduction products separately.

5.3. Modeling on cathode surfaces

The crystal structure of LiNiO$_2$ [$R\bar{3}m$] was taken from the Material Project database (ID: mp-554862).[97] The bulk crystal volume and atom positions were reoptimized with VASP 5.2.2 using the PBE+*U* functional, 520 eV cutoff, and a Methfessel–Paxton

This journal is © The Royal Society of Chemistry 2019

Energy Environ. Sci., 2019, **12**, 780–794 | 791

k-point mesh of $5 \times 5 \times 1$.[98] The U parameter was set to 6.37 eV as reported in Giordano et al.[78] In all calculations, a 0.2 eV 1st order Methfessel–Paxton broadening function was used and all structures were initialized in a ferromagnetic state with 3 (2.25, if 3 was unstable) μ_B assigned to Ni and 0.6 μ_B to everything else. Lithium was modeled with the '_sv' potential variant that considers the 1s electrons as valence, all other atoms used the standard set of potentials.

The supercell utility was used to generate all symmetry-unique configurations of half-lithiated structures using a $2 \times 2 \times 2$ size unit cell (this has 6 layers along the c-axis instead of 3).[99] The $R\bar{3}m$ spacegroup was assumed based on prior work.[78,100] Only 86 of the generated structures were optimized as above. The highly degenerate structures were discarded as the Li are far less homogenously distributed. The best structure was found to be one in which every other Li site was vacant, the cif file can be found in the ESI.†

Surface slabs were generated with the atomic simulation environment by cutting along the (1 0 4) direction.[101] Slabs were made to a thickness of 4 layers and approximately square in their interfacial dimensions (11.6104 Å by 11.8228 Å for $LiNiO_2$ and 11.4785 Å by 11.6535 Å for $Li_{0.5}NiO_2$). Vacuum was added to 24 Å in the perpendicular axis (about $3\times$ the height of 4 layers). For optimization, the bottom two layers were fixed to their bulk positions. A dipole correction along the extended axis was added for all surface calculations. All surface calculations considered only the Γ-point and used a 400 eV cutoff. All other considerations were unmodified except those to accelerate converge for slabs (i.e., the mixing parameters).

Conflicts of interest

There are no conflicts of interest to declare.

Acknowledgements

References

1 K. Xu, Chem. Rev., 2004, 104, 4303–4417.

2 K. Xu, Chem. Rev., 2014, 114, 11503–11618.

3 E. Peled, J. Electrochem. Soc., 1979, 126, 2047.

4 M. D. Tikekar, S. Choudhury, Z. Tu and L. A. Archer, Nat. Energy, 2016, 1, 16114.

5 A. O. Raji, R. Villegas Salvatierra, N. D. Kim, X. Fan, Y. Li, G. A. L. Silva, J. Sha and J. M. Tour, ACS Nano, 2017, 11, 6362–6369.

6 G. Zheng, S. W. Lee, Z. Liang, H. W. Lee, K. Yan, H. Yao, H. Wang, W. Li, S. Chu and Y. Cui, Nat. Nanotechnol., 2014, 9, 618–623.

7 D. Lin, Y. Liu, Z. Liang, H. W. Lee, J. Sun, H. Wang, K. Yan, J. Xie and Y. Cui, Nat. Nanotechnol., 2016, 11, 626–632.

8 S. Wei, Z. Cheng, P. Nath, M. D. Tikekar, G. Li and L. A. Archer, Sci. Adv., 2018, 4, 1–8.

9 T. Thompson, A. Sharafi, M. D. Johannes, A. Huq, J. L. Allen, J. Wolfenstine and J. Sakamoto, Adv. Energy Mater., 2015, 5, 1500096.

10 D. Gordon, M. Y. Wu, A. Ramanujapuram, J. Benson, J. T. Lee, A. Magasinski, N. Nitta, C. Huang and G. Yushin, Adv. Energy Mater., 2016, 6, 1501805.

11 N. J. Dudney, J. Power Sources, 2000, 89, 176–179.

12 A. Sharafi, E. Kazyak, A. L. Davis, S. H. Yu, T. Thompson, D. J. Siegel, N. P. Dasgupta and J. Sakamoto, Chem. Mater., 2017, 29, 7961–7968.

13 A. C. Kozen, C. F. Lin, A. J. Pearse, M. A. Schroeder, X. Han, L. Hu, S. B. Lee, G. W. Rubloff and M. Noked, ACS Nano, 2015, 9, 5884–5892.

14 Y. Liu, D. Lin, Z. Liang, J. Zhao, K. Yan and Y. Cui, Nat. Commun., 2016, 7, 10992.

15 R. Younesi, G. M. Veith, P. Johansson, K. Edström and T. Vegge, Energy Environ. Sci., 2015, 8, 1905–1922.

16 S. K. Jeong, H. Y. Seo, D. H. Kim, H. K. Han, J. G. Kim, Y. B. Lee, Y. Iriyama, T. Abe and Z. Ogumi, Electrochem. Commun., 2008, 10, 635–638.

17 X. Fan, L. Chen, O. Borodin, X. Ji, J. Chen, S. Hou, T. Deng, J. Zheng, C. Yang, S. C. Liou, K. Amine, K. Xu and C. Wang, Nat. Nanotechnol., 2018, 13, 715–722.

18 L. Suo, W. Xue, M. Gobet, S. G. Greenbaum, C. Wang, Y. Chen, W. Yang, Y. Li and J. Li, Proc. Natl. Acad. Sci. U. S. A., 2018, 115, 1156–1161.

19 M. S. Park, S. B. Ma, D. J. Lee, D. Im, S. G. Doo and O. Yamamoto, Sci. Rep., 2014, 4, 3815.

20 D. Aurbach, E. Zinigrad, Y. Cohen and H. Teller, Solid State Ionics, 2002, 148, 405–416.

21 F. Ding, W. Xu, X. L. Chen, J. Zhang, M. H. Engelhard, Y. H. Zhang, B. R. Johnson, J. V. Crum, T. A. Blake, X. J. Liu and J. G. Zhang, J. Electrochem. Soc., 2013, 160, A1894–A1901.

22 T. R. Jow, K. Xu, O. Borodin and U. Makoto, Electrolytes for lithium and lithium-ion batteries, Springer, 2014.

23 H. Kim, F. X. Wu, J. T. Lee, N. Nitta, H. T. Lin, M. Oschatz, W. I. Cho, S. Kaskel, O. Borodin and G. Yushin, *Adv. Energy Mater.*, 2015, **5**, 1401792.

24 J. Wang, Y. Yamada, K. Sodeyama, C. H. Chiang, Y. Tateyama and A. Yamada, *Nat. Commun.*, 2016, **7**, 12032.

25 J. Alvarado, M. A. Schroeder, M. H. Zhang, O. Borodin, E. Gobrogge, M. Olguin, M. S. Ding, M. Gobet, S. Greenbaum, Y. S. Meng and K. Xu, *Mater. Today*, 2018, **21**, 341–353.

26 X. D. Ren, S. R. Chen, H. Lee, D. H. Mei, M. H. Engelhard, S. D. Burton, W. G. Zhao, J. M. Zheng, Q. Y. Li, M. S. Ding, M. Schroeder, J. Alvarado, K. Xu, Y. S. Meng, J. Liu, J. G. Zhang and W. Xu, *Chem*, 2018, **4**, 1877–1892.

27 J. Qian, W. A. Henderson, W. Xu, P. Bhattacharya, M. Engelhard, O. Borodin and J. G. Zhang, *Nat. Commun.*, 2015, **6**, 6362.

28 P. Albertus, S. Babinec, S. Litzelman and A. Newman, *Nat. Energy*, 2018, **3**, 16–21.

29 X. L. Fan, L. Chen, X. Ji, T. Deng, S. Y. Hou, J. Chen, J. Zheng, F. Wang, J. J. Jiang, K. Xu and C. S. Wang, *Chem*, 2018, **4**, 174–185.

30 R. Miao, J. Yang, X. Feng, H. Jia, J. Wang and Y. Nuli, *J. Power Sources*, 2014, **271**, 291–297.

31 L. Grande, J. von Zamory, S. L. Koch, J. Kalhoff, E. Paillard and S. Passerini, *ACS Appl. Mater. Interfaces*, 2015, **7**, 5950–5958.

32 K. N. Wood, E. Kazyak, A. F. Chadwick, K. H. Chen, J. G. Zhang, K. Thornton and N. P. Dasgupta, *ACS Cent. Sci.*, 2016, **2**, 790–801.

33 P. Bai, J. Li, F. R. Brushett and M. Z. Bazant, *Energy Environ. Sci.*, 2016, **9**, 3221–3229.

34 Z. C. Devika Sirohi, L. Sun, T. Klose, T. C. Pierson, M. G. Rossmann and R. J. Kuhn, *Science*, 2016, **352**, 467–470.

35 A. Bartesaghi, A. Merk, S. Banerjee, D. Matthies, X. Wu, J. L. Milne and S. Subramaniam, *Science*, 2015, **348**, 1147–1151.

36 X. C. Bai, G. McMullan and S. H. W. Scheres, *Trends Biochem. Sci.*, 2015, **40**, 49–57.

37 Y. Li, Y. Li, A. Pei, K. Yan, Y. Sun, C.-L. Wu, L.-M. Joubert, R. Chin, A. L. Koh, Y. Yu, J. Perrino, B. Butz, S. Chu and Y. Cui, *Science*, 2017, **358**, 506.

38 X. Wang, M. Zhang, J. Alvarado, S. Wang, M. Sina, B. Lu, J. Bouwer, W. Xu, J. Xiao, J. G. Zhang, J. Liu and Y. S. Meng, *Nano Lett.*, 2017, **17**, 7606–7612.

39 M. J. Zachman, Z. Tu, S. Choudhury, L. A. Archer and L. F. Kourkoutis, *Nature*, 2018, **560**, 345–349.

40 K. Yoshida, M. Nakamura, Y. Kazue, N. Tachikawa, S. Tsuzuki, S. Seki, K. Dokko and M. Watanabe, *J. Am. Chem. Soc.*, 2011, **133**, 13121–13129.

41 J. Qian, B. D. Adams, J. Zheng, W. Xu, W. A. Henderson, J. Wang, M. E. Bowden, S. Xu, J. Hu and J.-G. Zhang, *Adv. Funct. Mater.*, 2016, **26**, 7094–7102.

42 S. Jiao, X. Ren, R. Cao, M. Engelhard, Y. Liu, D. Hu, D. Mei, J. Zheng, W. Zhao, Q. Li, N. Liu, B. D. Adams, C. Ma, J. Liu, J.-G. Zhang and W. Xu, Stable cycling of high-voltage lithium metal batteries in ether electrolytes, 2018.

43 K. Ueno, K. Yoshida, M. Tsuchiya, N. Tachikawa, K. Dokko and M. Watanabe, *J. Phys. Chem. B*, 2012, **116**, 11323–11331.

44 A. Petronico, T. P. Moneypenny, 2nd, B. G. Nicolau, J. S. Moore, R. G. Nuzzo and A. A. Gewirth, *J. Am. Chem. Soc.*, 2018, **140**, 7504–7509.

45 F. Wohde, M. Balabajew and B. Roling, *J. Electrochem. Soc.*, 2016, **163**, A714–A721.

46 V. Lesch, S. Jeremias, A. Moretti, S. Passerini, A. Heuer and O. Borodin, *J. Phys. Chem. B*, 2014, **118**, 7367–7375.

47 D. Aurbach, Y. Talyosef, B. Markovsky, E. Markevich, E. Zinigrad, L. Asraf, J. S. Gnanaraj and H. J. Kim, *Electrochim. Acta*, 2004, **50**, 247–254.

48 D. Aurbach, M. L. Daroux, P. W. Faguy and E. Yeager, *J. Electrochem. Soc.*, 1987, **134**, 1611–1620.

49 Y. Zhang, J. Qian, W. Xu, S. M. Russell, X. Chen, E. Nasybulin, P. Bhattacharya, M. H. Engelhard, D. Mei, R. Cao, F. Ding, A. V. Cresce, K. Xu and J. G. Zhang, *Nano Lett.*, 2014, **14**, 6889–6896.

50 J. Z. Lee, T. A. Wynn, M. A. Schroeder, J. Alvarado, X. Wang, K. Xu and Y. S. Meng, *ACS Energy Lett.*, 2019, 489–493.

51 H. Liu, X. Wang, H. Zhou, H.-D. Lim, X. Xing, Q. Yan, Y. S. Meng and P. Liu, *ACS Appl. Energy Mater.*, 2018, 1864–1869.

52 D. Aurbach and Y. Gofer, *J. Electrochem. Soc.*, 1991, **138**, 3529–3536.

53 D. Aurbach, I. Weissman, A. Schechter and H. Cohen, *Langmuir*, 1996, **12**, 3991–4007.

54 L. E. Camacho-Forero, T. W. Smith and P. B. Balbuena, *J. Phys. Chem. C*, 2016, **121**, 182–194.

55 L. E. Camacho-Forero and P. B. Balbuena, *Phys. Chem. Chem. Phys.*, 2017, **19**, 30861–30873.

56 L. E. Camacho-Forero, T. W. Smith, S. Bertolini and P. B. Balbuena, *J. Phys. Chem. C*, 2015, **119**, 26828.

57 A. Budi, A. Basile, G. Opletal, A. F. Hollenkamp, A. S. Best, R. J. Rees, A. I. Bhatt, A. P. O'Mullane and S. P. Russo, *J. Phys. Chem. C*, 2012, **116**, 19789–19797.

58 H. Yildirim, J. B. Haskins, C. W. Bauschlicher and J. W. Lawson, *J. Phys. Chem. C*, 2017, **121**, 28214–28234.

59 Y. Li, K. Leung and Y. Qi, *Acc. Chem. Res.*, 2016, **49**, 2363–2370.

60 A. Wang, S. Kadam, H. Li, S. Shi and Y. Qi, *npj Comput. Mater.*, 2018, **4**, 15.

61 K. Leung and K. L. Jungjohann, *J. Phys. Chem. C*, 2017, **121**, 20188–20196.

62 Z. Liu, Y. Qi, Y. X. Lin, L. Chen, P. Lu and L. Q. Chen, *J. Electrochem. Soc.*, 2016, **163**, A592–A598.

63 E. Markevich, R. Sharabi, V. Borgel, H. Gottlieb, G. Salitra, D. Aurbach, G. Semrau and M. A. Schmidt, *Electrochim. Acta*, 2010, **55**, 2687–2696.

64 D. Molina Piper, T. Evans, K. Leung, T. Watkins, J. Olson, S. C. Kim, S. S. Han, V. Bhat, K. H. Oh, D. A. Buttry and S. H. Lee, *Nat. Commun.*, 2015, **6**, 6230.

65 M. Wang, L. Huai, G. Hu, S. Yang, F. Ren, S. Wang, Z. Zhang, Z. Chen, Z. Peng, C. Shen and D. Wang, *J. Phys. Chem. C*, 2018, **122**, 9825–9834.

66 C. Park, M. Kanduč, R. Chudoba, A. Ronneburg, S. Risse, M. Ballauff and J. Dzubiella, *J. Power Sources*, 2018, **373**, 70–78.

This journal is © The Royal Society of Chemistry 2019

Energy Environ. Sci., 2019, **12**, 780–794 | 793

67 J. Vatamanu and O. Borodin, *J. Phys. Chem. Lett.*, 2017, **8**, 4362–4367.

68 L. Suo, O. Borodin, T. Gao, M. Olguin, J. Ho, X. Fan, C. Luo, C. Wang and K. Xu, *Science*, 2015, **350**, 938–943.

69 L. Suo, O. Borodin, W. Sun, X. Fan, C. Yang, F. Wang, T. Gao, Z. Ma, M. Schroeder, A. von Cresce, S. M. Russell, M. Armand, A. Angell, K. Xu and C. Wang, *Angew. Chem., Int. Ed. Engl.*, 2016, **55**, 7136–7141.

70 R. Miao, J. Yang, Z. Xu, J. Wang, Y. Nuli and L. Sun, *Sci. Rep.*, 2016, **6**, 21771.

71 Z. L. Brown, S. Jurng and B. L. Lucht, *J. Electrochem. Soc.*, 2017, **164**, A2186–A2189.

72 J. M. Zheng, P. F. Yan, D. H. Mei, M. H. Engelhard, S. S. Cartmell, B. J. Polzin, C. M. Wang, J. G. Zhang and W. Xu, *Adv. Energy Mater.*, 2016, **6**, 1502151.

73 R. A. Quinlan, Y.-C. Lu, D. Kwabi, Y. Shao-Horn and A. N. Mansour, *J. Electrochem. Soc.*, 2016, **163**, A300–A308.

74 J. Alvarado, C. Ma, S. Wang, K. Nguyen, M. Kodur and Y. S. Meng, *ACS Appl. Mater. Interfaces*, 2017, **9**, 26518–26530.

75 G. Yan, X. Li, Z. Wang, H. Guo, W. Peng and Q. Hu, *J. Solid State Electrochem.*, 2015, **20**, 507–516.

76 Y. Diao, K. Xie, S. Z. Xiong and X. B. Hong, *J. Electrochem. Soc.*, 2012, **159**, A1816–A1821.

77 T. M. Østergaard, L. Giordano, I. E. Castelli, F. Maglia, B. K. Antonopoulos, Y. Shao-Horn and J. Rossmeisl, *J. Phys. Chem. C*, 2018, **122**, 10442–10449.

78 L. Giordano, P. Karayaylali, Y. Yu, Y. Katayama, F. Maglia, S. Lux and Y. Shao-Horn, *J. Phys. Chem. Lett.*, 2017, **8**, 3881–3887.

79 O. Borodin, L. Suo, M. Gobet, X. Ren, F. Wang, A. Faraone, J. Peng, M. Olguin, M. Schroeder, M. S. Ding, E. Gobrogge, A. von Wald Cresce, S. Munoz, J. A. Dura, S. Greenbaum, C. Wang and K. Xu, *ACS Nano*, 2017, **11**, 10462–10471.

80 L. Giordano, P. Karayaylali, Y. Yu, Y. Katayama, F. Maglia, S. Lux and Y. Shao-Horn, *J. Phys. Lett.*, 2017, **8**, 3881–3887.

81 W. Lu, J. Zhang, J. Xu, X. Wu and L. Chen, *ACS Appl. Mater. Interfaces*, 2017, **9**, 19313–19318.

82 J.-N. Zhang, Q. Li, Y. Wang, J. Zheng, X. Yu and H. Li, *Energy Storage Mater.*, 2018, **14**, 1–7.

83 W. T. Gu, O. Borodin, B. Zdyrko, H. T. Lin, H. Kim, N. Nitta, J. X. Huang, A. Magasinski, Z. Milicev, G. Berdichevsky and G. Yushin, *Adv. Funct. Mater.*, 2016, **26**, 1507–1516.

84 O. Borodin, X. Ren, J. Vatamanu, A. V. W. Cresce, J. Knap and K. Xu, *Acc. Chem. Res.*, 2017, **50**, 2886–2894.

85 K. Leung, *Chem. Mater.*, 2017, **29**, 2550–2562.

86 D. J. Xiong, R. Petibon, M. Nie, L. Ma, J. Xia and J. R. Dahn, *J. Electrochem. Soc.*, 2016, **163**, A546–A551.

87 J. Hutter, M. Iannuzzi, F. Schiffmann and J. VandeVondele, *Wiley Interdiscip. Rev.: Comput. Mol. Sci.*, 2014, **4**, 15–25.

88 J. P. Perdew, K. Burke and M. Ernzerhof, *Phys. Rev. Lett.*, 1996, **77**, 3865–3868.

89 S. Goedecker, M. Teter and J. Hutter, *Phys. Rev. B: Condens. Matter Mater. Phys.*, 1996, **54**, 1703–1710.

90 C. Hartwigsen, S. Goedecker and J. Hutter, *Phys. Rev. B: Condens. Matter Mater. Phys.*, 1998, **58**, 3641–3662.

91 J. VandeVondele and J. Hutter, *J. Chem. Phys.*, 2007, **127**, 114105.

92 S. Grimme, S. Ehrlich and L. Goerigk, *J. Comput. Chem.*, 2011, **32**, 1456–1465.

93 M. Verstraete and X. Gonze, *Phys. Rev. B: Condens. Matter Mater. Phys.*, 2001, **65**, 035111.

94 K. Momma and F. Izumi, *J. Appl. Crystallogr.*, 2011, **44**, 1272–1276.

95 W. Humphrey, A. Dalke and K. Schulten, *J. Mol. Graphics*, 1996, **14**(33-38), 27–38.

96 A. Jones and B. Leimkuhler, *J. Chem. Phys.*, 2011, **135**, 084125.

97 A. Jain, S. P. Ong, G. Hautier, W. Chen, W. D. Richards, S. Dacek, S. Cholia, D. Gunter, D. Skinner, G. Ceder and K. A. Persson, *APL Mater.*, 2013, **1**, 011002.

98 J. Hafner, *J. Comput. Chem.*, 2008, **29**, 2044–2078.

99 K. Okhotnikov, T. Charpentier and S. Cadars, *J. Cheminf.*, 2016, **8**, 17.

100 K. Chang, B. Hallstedt and D. Music, *CALPHAD: Comput. Coupling Phase Diagrams Thermochem.*, 2012, **37**, 100–107.

101 A. H. Larsen, J. J. Mortensen, J. Blomqvist, I. E. Castelli, R. Christensen, M. Dułak, J. Friis, M. N. Groves, B. Hammer and C. Hargus, *J. Phys.: Condens. Matter*, 2017, **29**, 273002.